Petroleum Science 22 (2025) 850–867

Contents lists available at ScienceDirect

Petroleum Science

journal homepage: www.keaipublishing.com/en/journals/petroleum-science

Original Paper

Factors and detection capability of look-ahead logging while drilling (LWD) tools

Ran-Ming Liu [a, b, c], Wen-Xiu Zhang [a, b, c, *], Wen-Xuan Chen [a, b, c], Peng-Fei Liang [a, b, c], Xing-Han Li [a, b, c], Zhi-Xiong Tong [a, b, c]

[a] *State Key Laboratory of Deep Petroleum Intelligent Exploration and Development, Institute of Geology and Geophysics, Chinese Academy of Sciences, Beijing, 100029, China*
[b] *Innovation Academy for Earth Science, CAS, Beijing, 100029, China*
[c] *University of Chinese Academy of Sciences, Beijing, 100049, China*

ARTICLE INFO

Article history:
Received 10 July 2024
Received in revised form
25 December 2024
Accepted 25 December 2024
Available online 26 December 2024

Edited by Jia-Jia Fei

Keywords:
Logging while drilling
Look-ahead
Deep reading
Air-sea test
Boundary detection

ABSTRACT

Electromagnetic technology used in logging while drilling (LWD) provides the resistivity distribution around a borehole within a range of several tens of meters. However, a blind zone appears in front of the drill bit when operating in high-angle wells, limiting the ability to detect formations ahead of the drill bit. Look-ahead technology addresses this issue and substantially enhances the proactive capability of geological directional drilling. In this study, we examine the detection capabilities of various component combinations of magnetic dipole antenna. Based on the sensitivity of each component to the axial information, a coaxial component is selected as a boundary indicator. We investigate the impact of various factors, such as frequency and transmitter and receiver (TR) distance, under different geological models. This study proposes 5 and 20 kHz as appropriate frequencies, and 10–14 and 12–17 m as suitable TR distance combinations. The accuracy of the numerical calculation results is verified via air-sea testing, confirming the instrument's detection capability. A test model that eliminated the influence of environmental factors and seawater depth is developed. The results have demonstrated that the tool can recognize the interface between layers up to 21.6 m ahead. It provides a validation idea for the design of new instruments as well as the validation of detection capabilities.

1. Introduction

Geosteering drilling technology uses real-time geological measurements to guide well trajectories, enabling more efficient penetration of oil and gas reservoirs (Li et al., 2005; Lin et al., 2021). As the exploration of complex oil and gas reservoirs intensifies, the logging industry faces challenges such as wellbore optimization and the inherent limitations of logging while drilling (LWD) (Seydoux et al., 2014). The industry has increasingly relied on geosteering technologies to achieve optimal landings and trajectories for horizontal wells (Meador, 2009; Larsen et al., 2016). LWD electromagnetic technology identifies geological boundaries by measuring the electrical contrast near the wellbore and plays a crucial role in geosteering. This technology has substantially enhanced the accuracy of structural and reservoir assessment, thereby improving drilling encounters, success, and recovery rates (Teruhiko and Song, 2001; Omeragic et al., 2005). Traditional LWD electromagnetic logging instruments use compensatory measurement methods (Su, 2005). Axial transceiver coils measure the resistivity around the wellbore but lack directional sensitivity, making it difficult to determine the relative positions of the formation and wellbore (Meyer et al., 1994; Bittar, 2000). Advances in LWD azimuthal electromagnetic instruments have introduced orthogonal or inclined coil structures which enhance directional sensitivity and extend the detection depths to 5–6 m (Bittar, 2009; Wang et al., 2022). Despite these advancements, the risk of drilling beyond the formation persists. Current technologies fail to meet the detection requirements for multilayer structures and distant anomalies encountered during production and development.

In recent decades, there have been considerable advancements in resistivity measurement technology. In 2015, Schlumberger introduced the Geosphere instrument for long-distance detection,

---

* Corresponding author.
E-mail address: zhangwenxiu@mail.iggcas.ac.cn (W.-X. Zhang).

https://doi.org/10.1016/j.petsci.2024.12.024
1995-8226/

which was applied to horizontal well landing operations in the Bohai Oilfield (Guo et al., 2020). Despite the developed sand bodies, the target layer was detected approximately 28 m below during the landing process (Li et al., 2019). Halliburton and Baker Hughes also developed ultra-deep detection instruments, namely, EarthStar and Visitrak (Constable et al., 2016). These technologies have enhanced the interpretation and evaluation of reservoir structures by extending investigation depths to several tens of meters. However, they have primarily measured radial distances with challenges in forward detection when the boundary angle exceeded 40° (Upchurch et al., 2015). Radial detection methods are constrained by geological variations and often make it difficult to maintain a drill bit within the target layer. Therefore, they may not fulfill the drilling measurement requirements. To address the demand for reliable measurements of formations ahead of the drill bit, the LWD look-ahead resistivity technology is developed. This technology has evolved from azimuthal resistivity logging and has provided true forward detection capabilities. It can detect electrical boundaries, oil-water interfaces, and anomalies below the drill bit (Constable et al., 2012; Yu et al., 2022). Instruments such as Schlumberger's Irisphere and Halliburton's BrightStar provide real-time detection of resistivity up to 100 feet (30 m) below the drill bit. This capability enhances the interpretation of reservoir structures and mitigates drilling risks (Wang et al., 2019).

In this study, we aim to investigate the use of a three-component magnetic dipole source that functions as both a transmitting and receiving antenna. We assess the detection capabilities by examining the attenuation in the measured voltage signals. The correlations among the transmission frequency, formation resistivity, transmitter and receiver (TR) distance, and detection capability are systematically analyzed. Owing to the unique structure of the look-ahead detection instrument, an air-sea test method is used for evaluation. Further, we have outlined the calibration process used to determine the detection capabilities. By analyzing the signal patterns within the detection range, we establish the conditions needed to mitigate environmental influences, and the corresponding physical model is defined. The conversion process between the test and standard models has been detailed. A comparative analysis of the detection capabilities of the test and standard models is presented to illustrate the effectiveness of this approach.

2. Theory

In this section, we explore the sensitivity of the electromagnetic LWD tool for axial information on the signal strength and attenuation. The influence of different models on the frequency, TR distance, and depth of detection (DoD) of the tool is examined. These insights form a foundation for parameter selection in instrument design.

2.1. Axial sensitivity

The LWD look-ahead resistivity instrument comprises one coil transmitter subset and two separate coil receiver subsets, each of which features a three-component antenna. The subs are connected using a nonmagnetic drill collar. The coils in the x, y, and z directions are arranged axially along the instrument, as shown in Fig. 1.

An LWD tool typically uses the attenuation of the magnetic field voltage signals to predict the formation boundary ahead of the drill bit, which is defined as

$$Att = 20\log_{10}\left(\frac{V_{\mathrm{R}_1}}{V_{\mathrm{R}_2}}\right) \tag{1}$$

where V_{R_1} and V_{R_2} represent the voltage signals measured using R_1 and R_2, respectively (see Fig. 1). The absolute values of Att vary significantly across different formation models. Normalization is essential for subtracting the amplitude value at the transmitter to the boundary (TTB) = 30 m. This normalization allows the 0.05 dB attenuation to be assessed using the 0 point as a baseline. The voltage measure in the receiving antenna (Zhang et al., 2004; Wang, 2011; Hong et al., 2018; Wang et al., 2020), which has N turns and an area S, is given by

$$V = |j\omega\mu NSH| \tag{2}$$

where $j = \sqrt{-1}$, μ denotes the magnetic permeability and ω represents the angular frequency. H is the magnetic fields excited by different transmitters and recorded by different receivers (Huang and Shen, 1989; Zhong et al., 2008; Fan et al., 2021) as:

$$\begin{bmatrix} H_{xx} & H_{xy} & H_{xz} \\ H_{yx} & H_{yy} & H_{yz} \\ H_{zx} & H_{zy} & H_{zz} \end{bmatrix} \tag{3}$$

Here, the subscripts i, j represent the magnetic fields excited by the i-direction transmitter and j-direction receiver, respectively. Owing to the rotational symmetry, the nine magnetic field components H can be simplified into four independent components (Liang et al., 2023). H_{xx}, H_{xz}, H_{zx}, and H_{zz}. DoD is defined as the distance between the transmitter and the boundary where the signal attenuation reaches its limit.

To illustrate the axial sensitivity in Fig. 2, which shows two scenarios: (a) fixing the TR distance at 10 m while varying the TTB, and (b) fixing the TTB at 5 m while varying the TR distance. Fig. 3(a) shows that as the tool gradually moves away from the interface, significant changes occur in the amplitudes of the four signals when the transmitter is within 5 m of the interface. However, when the distance exceeds 5 m, the signal strengths become almost identical to those of a uniform formation. The Vzx and Vxz trends are the opposite, and the coaxial components become stronger and more sensitive as the transmitter move away from the interface. The cross-component signals exhibit higher sensitivity to the TR distance than the coaxial component signals. Vzz is stronger when the TR distance is less than 5 m, whereas Vxx is significantly stronger than Vzz when the TR distance exceeded 5 m. We expect the signal to demonstrate sufficient sensitivity to axial variations. This implies that the attenuation intensity should be high. It is crucial to ensure that the signal intensity is sufficiently high. To investigate the detection capabilities, we use coaxial signals Vzz (VMD) and Vxx (HMD).

2.2. TR distance

To investigate the effects of various TR distance combinations on the detection capability, four model sets are used (Fig. 4). The instrument is assumed to be perpendicular to the formation interface and operate at a frequency of 20 kHz. The TTB range extends from 1 to 30 m. The definition of λ is the ratio of the resistivity of the formation where the instrument is located to the resistivity of the adjacent layer. The λ values for Models 1 through 4 are 100, 10, 0.1, and 0.01, respectively. The specific resistivity parameters are shown in Fig. 4.

The results from using the amplitude ratio to assess the detection capability for different TR distance combinations are shown in

Fig. 1. Three-component transceiver antenna structure of the LWD look-ahead resistivity instrument, where T represents the transmitting antenna, and R_1 and R_2 represent the first and second receiving antenna, respectively.

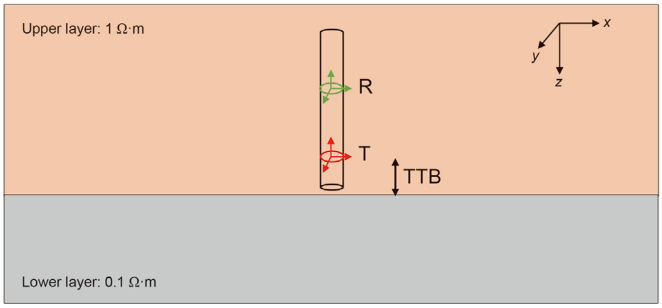

Fig. 2. Inhomogeneous formation model. The upper layer has a resistivity of 1 Ω•m, and the lower layer has a resistivity of 0.1 Ω•m.

Fig. 5. Vertical axes represent TR_1, while the horizontal axis represents R_1R_2. Under the same conditions, the HMD component exhibits a slightly greater DoD than the VMD component. Both DoD and the pattern of amplitude variation are influenced by λ. The greater the λ value, the deeper the detection depth is achieved. Model 1 achieved a greater detection depth than Model 2, and Model 4 achieved a greater detection depth than Model 3.

As TR_1 and R_1R_2 increased in Model 1, the detection capability improved. The maximum detection distance with the VMD is 23 m ahead of the transmitter, whereas the HMD achieves a detection depth of 26 m. However, as λ decreases, the detection capability gradually decreases. The optimal parameter range for achieving the maximum detection depth shifts toward shorter TR distances. In Model 2, the maximum detection depth is only 10 m, and the corresponding TR_1 is less than 5 m. If the instrument is located in a low-resistivity layer, the detection depth is less than 4 m. The contrast in resistivity between the layers has a minimal effect on the detection capability. The observed patterns for both signal components show that as TR_1 decreases, the detection capability improves.

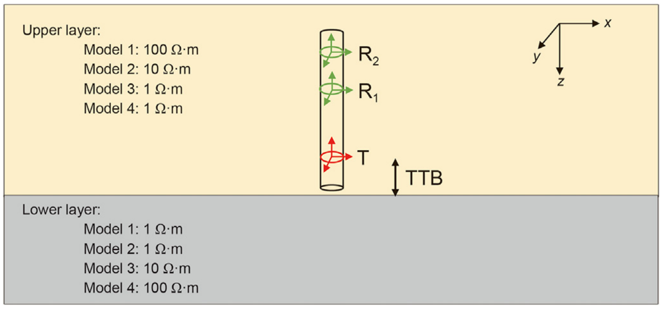

Fig. 4. Two-layer formation model. Model 1: The upper layer is 100 Ω·m and the lower layer is 1 Ω·m. Model 2: The upper layer is 10 Ω·m and the lower layer is 1 Ω·m. Model 3: The upper layer is 1 Ω·m and the lower layer is 10 Ω·m. Model 4: The upper layer is 1 Ω·m and the lower layer is 100 Ω·m.

Fig. 6 illustrates the relationship between the TR distance and received signal amplitude. The results indicate that the amplitude decreases rapidly as the TR distance increases. When the distance increases from 10 to 20 m, the amplitude is reduced by a factor of 100. Under the same conditions, adding TTB also reduces the amplitude but at a much slower rate than the change in TR distance. Therefore, to ensure the strength of the received signals, it is important to focus on the effect of the TR distance.

In Model 1, DoD increases as TR_1 and R_1R_2 increase. However,

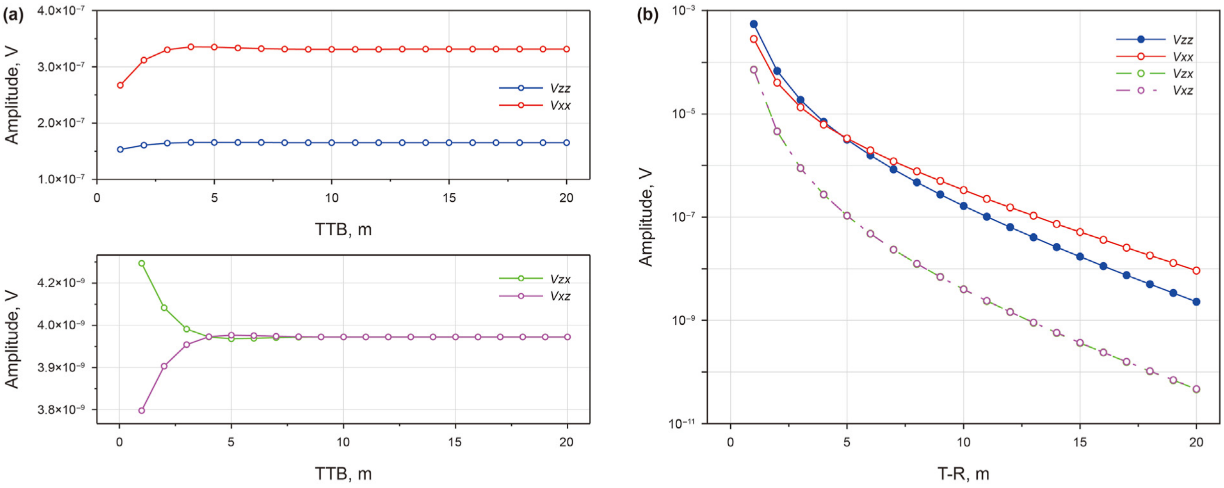

Fig. 3. The axial sensitivity of magnetic field signal components. (**a**) The effect of TTB on signal amplitude; (**b**) The effect of TR distance on signal amplitude.

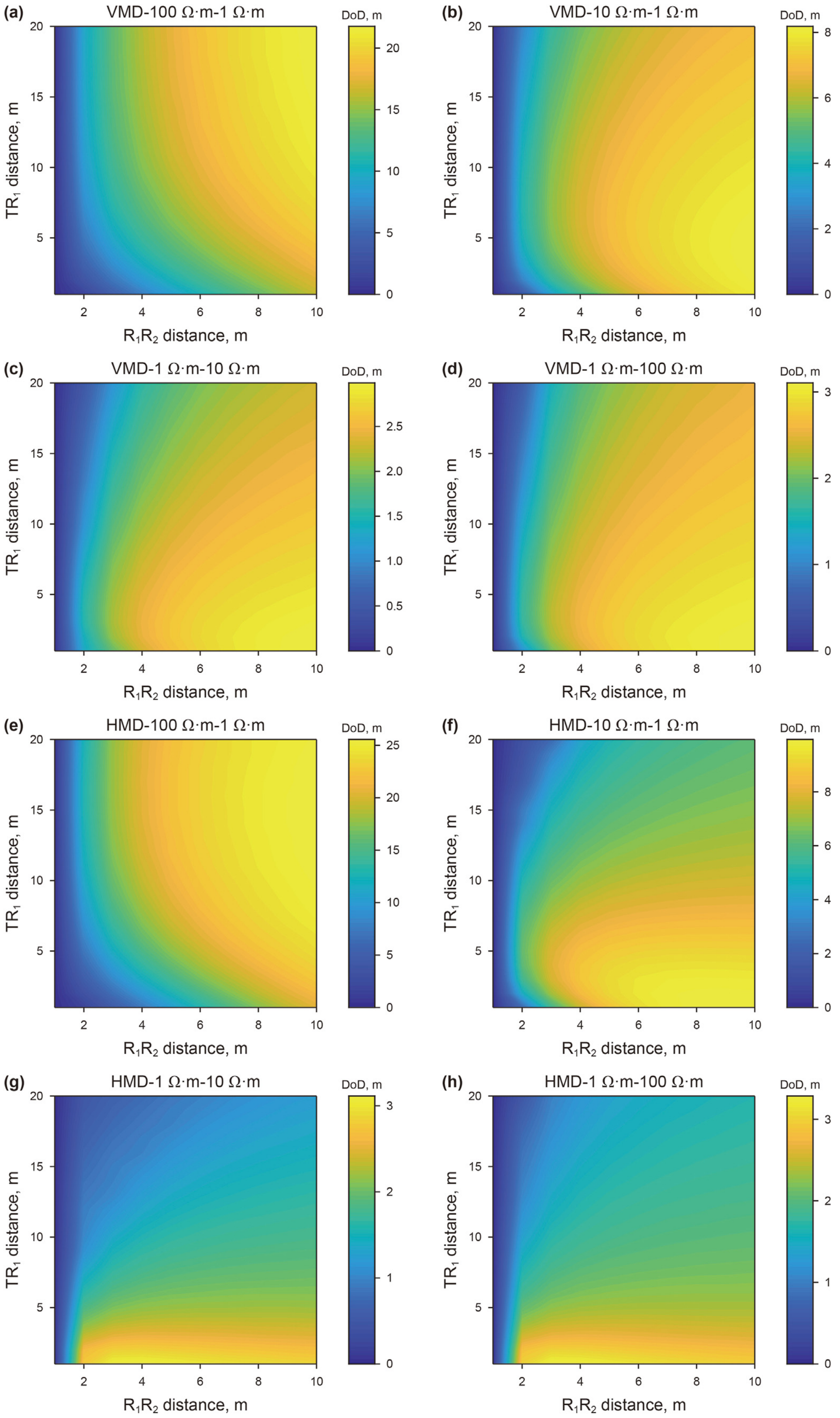

Fig. 5. DoD corresponds to TR distance in different models, (**a**)–(**d**) for VMD and (**e**)–(**h**) for HMD.

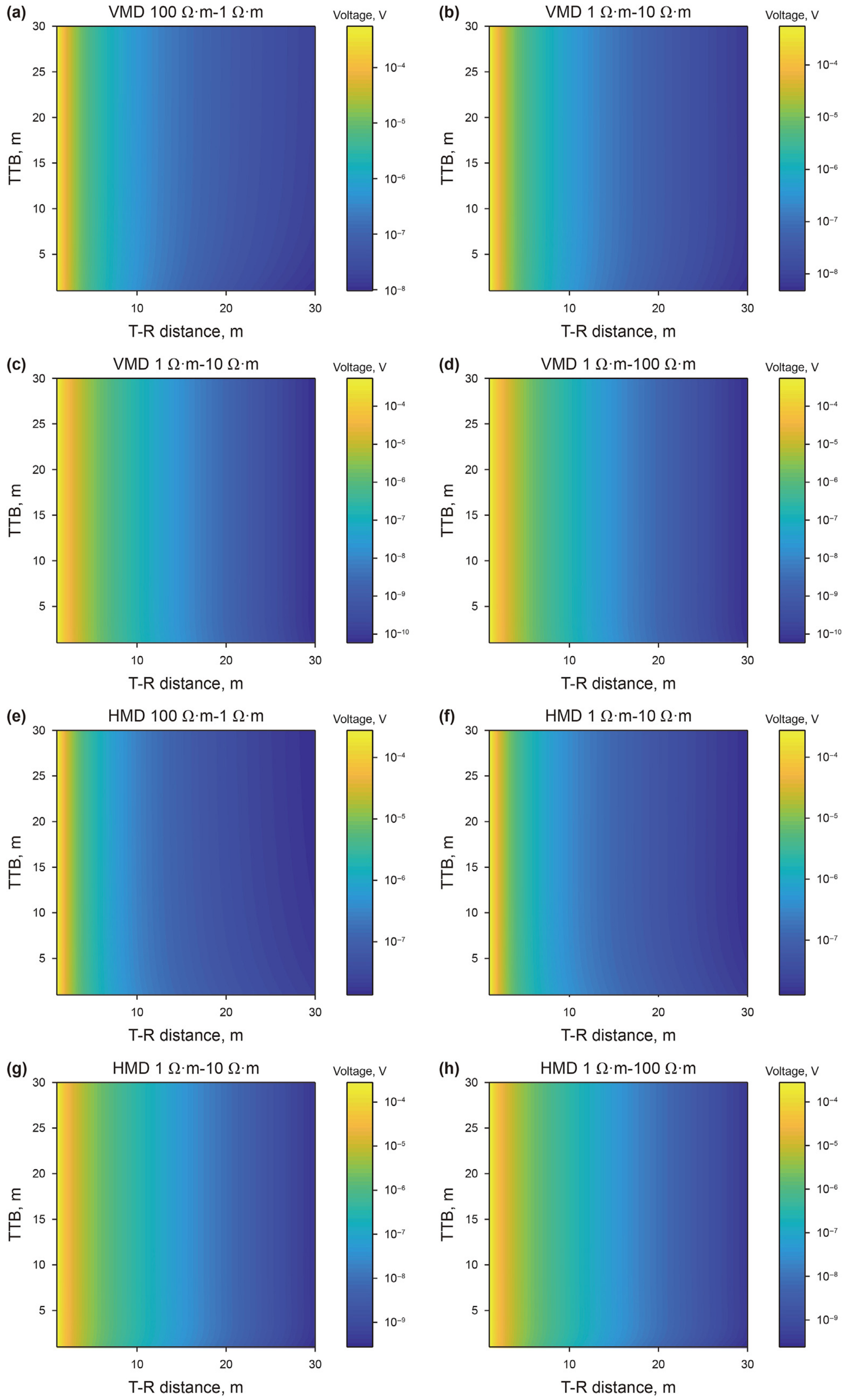

Fig. 6. Amplitude corresponds to TR distance in different models, (**a**)–(**d**) for VMD and (**e**)–(**h**) for HMD.

from a design perspective, it is crucial to maintain size within practical limits. Excessively long instruments may prove inconvenient. Furthermore, increasing the TR distance results in a reduction in the amplitude. Thus, it is pertinent to consider the amplitude ratio within the effective receiving range because it indicates the maximum viable detection depth. For example, if TR_1 is set to 10 m, TR_2 should be adjusted to 20 m to optimize the detection depth. Nevertheless, the amplitude at R_2 (below 0.1 μV) can easily be obscured by environmental noise even after amplification. Therefore, the selection of the TR distance must consider both the strength and the amplitude ratio.

With an input current of 0.1 A and both the transmitter and receiver antenna having 100 turns, considering a metal drill collar and a minimum detectable signal strength of 100 nV, the maximum detection distance (TR_{max}) can be determined from Fig. 6. Therefore, it is appropriate to select the TR distance combination where $TR_1 + TR_2 < TR_{max}$ (Fig. 5). Here, the corresponding DoD represents the effective detection depth. Fig. 7 illustrates the effective DoD for various geological models. This demonstrates that R_1R_2 values greater than 6 m results in a larger DoD. Theoretically, using a combination of long and short TR distances, such as 2–7 m and 4–10 m, can yield significant penetration depths under various geological conditions (Zhang et al., 2018). Long-distance combinations are preferred for resistive formations, whereas short-distance combinations are more suitable for conductive formations.

However, the instrument's overall structure must be considered. The LWD system integrates various measurement instruments. It must measure the resistivity of the formation ahead of the bit to optimize the drilling trajectory and other parameters such as mud temperature and density (Pardo and Torres Verdín, 2015). Traditional resistivity instruments are typically installed between the transmitting and receiving antenna, with lengths typically exceeding 7 m. Consequently, it is crucial to ensure that TR_1 exceeds 7 m. Considering the structural constraints, the final selected antenna TR distance combinations are 10–14 m and 12–17 m.

2.3. Frequency

The frequency ranges from 500 to 100 kHz, and the TTB range is set from 1 to 30 m in the models, as shown in Fig. 8. The DoD is calculated at various frequencies using both long and short TR distances by using the amplitude ratio method. Fig. 8(a) and (b) illustrate the variation in the VMD component detection depth with frequency. Meanwhile, Fig. 8(c) and (d) depict the variation in the HMD. This figure shows the performance in the high-resistivity layers with red curves and in the low-resistivity layers with blue curves.

The DoD for both VMD and HMD initially increase and then decrease with increasing frequency. The frequency corresponding to the maximum detection depth decreases as λ decreases. In high-resistivity layers, the DoD of VMD can reach approximately 20 m. Variations in λ significantly affect the detection depth. In low-resistivity layers, the DoD for VMD is relatively shallow. At frequencies below 1 kHz, the maximum detection depth is limited to 10 m. Above 5 kHz, λ has minimal impact on detection depth, with noticeable differences occurring only at lower frequencies. The detection pattern of the HMD in the high-resistivity layers mirrors that of the VMD. However, the effect of λ on detection depth is minimal. The DoD in Models 2–4 are nearly identical to that in Model 1 and is only a few meters shallower. Furthermore, it is essential to analyze these patterns within the range of effective signal amplitudes.

With the TR distance set to 10 m, Fig. 9 illustrates the variations in the signal amplitude at different frequencies and TTB. The change patterns in signal strength for both VMD and HMD are similar. A higher λ corresponds to stronger signals, and signal amplitude increases with frequency. In the low-resistivity layers, the signal amplitude initially increases and then decreases with increasing frequency. The signals below 1 kHz are significantly lower than the minimum resolution. In the 10–80 kHz frequency range, the signals received are strong, but the detection range is more extensive in the 1–20 kHz range. Therefore, considering the combined variation patterns of frequency and DoD, frequencies of 5 and 20 kHz are selected. The lower frequency provides greater detection depth in high-resistivity layers with small λ or low-resistivity layers. Conversely, the higher frequency results in greater detection depth in high-resistivity layers with large λ.

2.4. Resistivity

We conduct a series of calculations to evaluate the effects of various TR distance combinations and frequencies on DoD across different geological models. The structure and minimum resolution of the tool are considered to define the appropriate conditions. The calculation results indicate that the tool perform effectively in high-resistivity formations. The boundaries are identified approximately 20 m from the interface. This distance provides sufficient space for the tool to be oriented or positioned. However, if the tool is placed in a low-resistivity formation, it is insufficient for effective geosteering. Its detection capability is significantly diminished, with a range of less than 5 m. Given the variable nature of the formation properties, it is crucial to evaluate the impact of different models on detection capabilities. This approach facilitates the understanding of the performance of a tool with specific characteristics across various formations (Liu et al., 2024). Fig. 10 presents the DoD for both long and short TR distances at frequencies of 5 and 20 kHz for the resistivities of the current and shoulder layers. The horizontal axis indicates the resistivity of the layer, while the vertical axis indicates the shoulder resistivity.

A region of limited detection capability for geological signals is evident along the diagonal section of the diagram where the detection capability approaches zero. The trends of DoD with λ are generally consistent between VMD and HMD, although some differences exist. When the tool is placed in a high-resistivity formation, VMD requires a higher resistivity value for the current layer and λ to achieve greater detection depth. In contrast, HMD achieves optimal performance when the resistivity of the current layer ranges from approximately 10 to 100 Ω·m. Additionally, the range of applicable resistivity values for HMD is broader. When a high-resistivity tool is used to identify a low-resistivity formation, the detection capability and applicable resistivity range are approximately equivalent for both methods. The detection depth of the HMD is slightly greater than that of the VMD. It decreases when resistivity exceeds 100 Ω·m, reaching approximately 15 m. Conversely, when a low-resistivity tool is used to detect high-resistivity formations, VMD is less than 10 m. In contrast, the HMD can detect interfaces ranging from 10 to 20 m, provides that the resistivity of the current layer is not too low and the resistivity of the shoulder layer is relatively high. HMD is more sensitive to formations with higher resistivity contrasts, even if the instrument is in a low-resistivity layer. This sensitivity is particularly important for industrial applications. The advantage of VMD lies in its ability to more accurately identify interfaces where the resistivity of the current layer is significant and the resistivity of the shoulder layer is not excessively low.

A frequency of 5 kHz is suitable for local layer resistances ranging from a few to several hundred Ω·m. A frequency of 20 kHz is suitable for formations with resistivities ranging from tens to hundreds of Ω·m. This suggests that the detection range for 5 kHz aligns more closely with actual underground conditions. However,

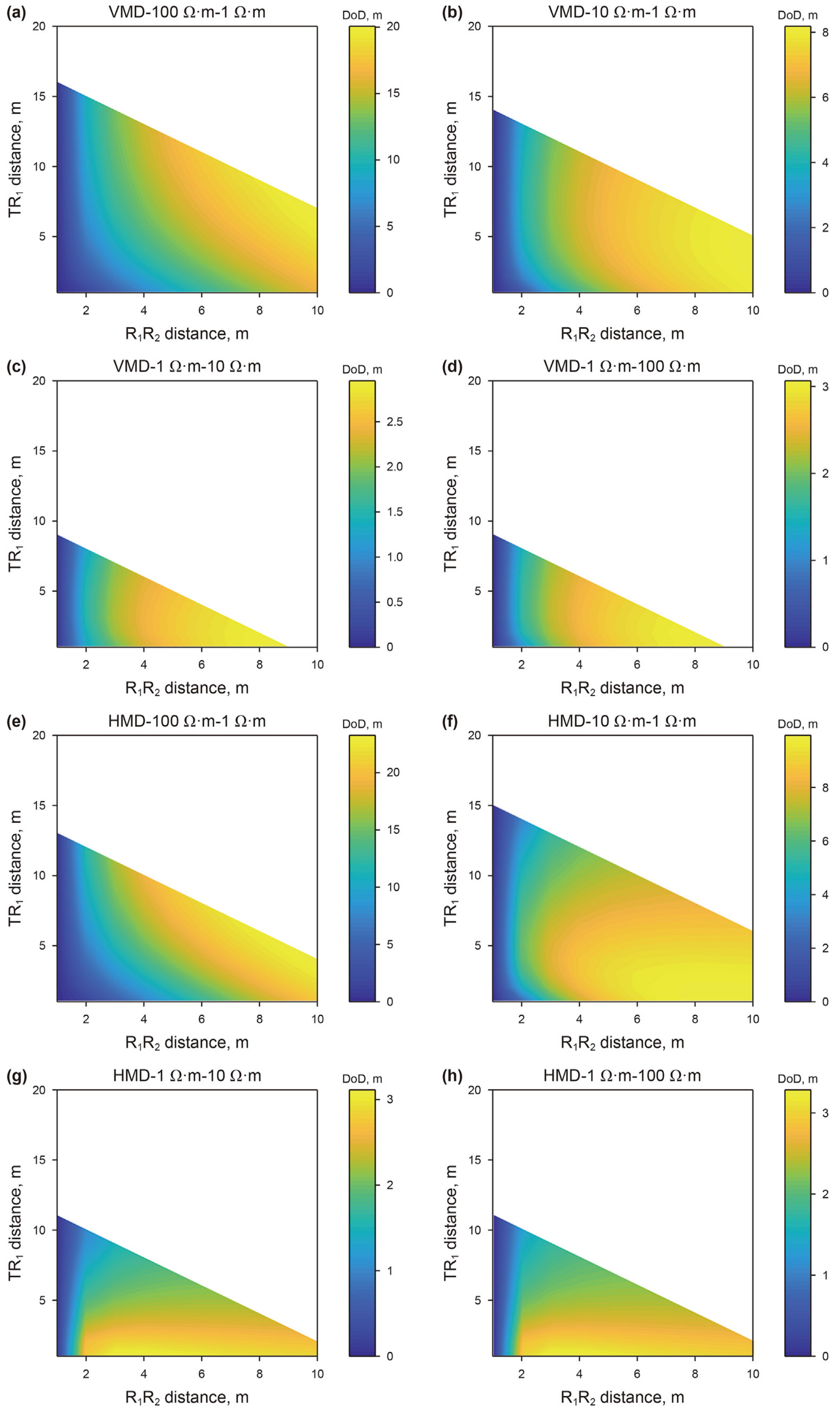

Fig. 7. Effective DoD corresponds to TR distance in different models, (**a**)–(**d**) for VMD, (**e**)–(**h**) for HMD.

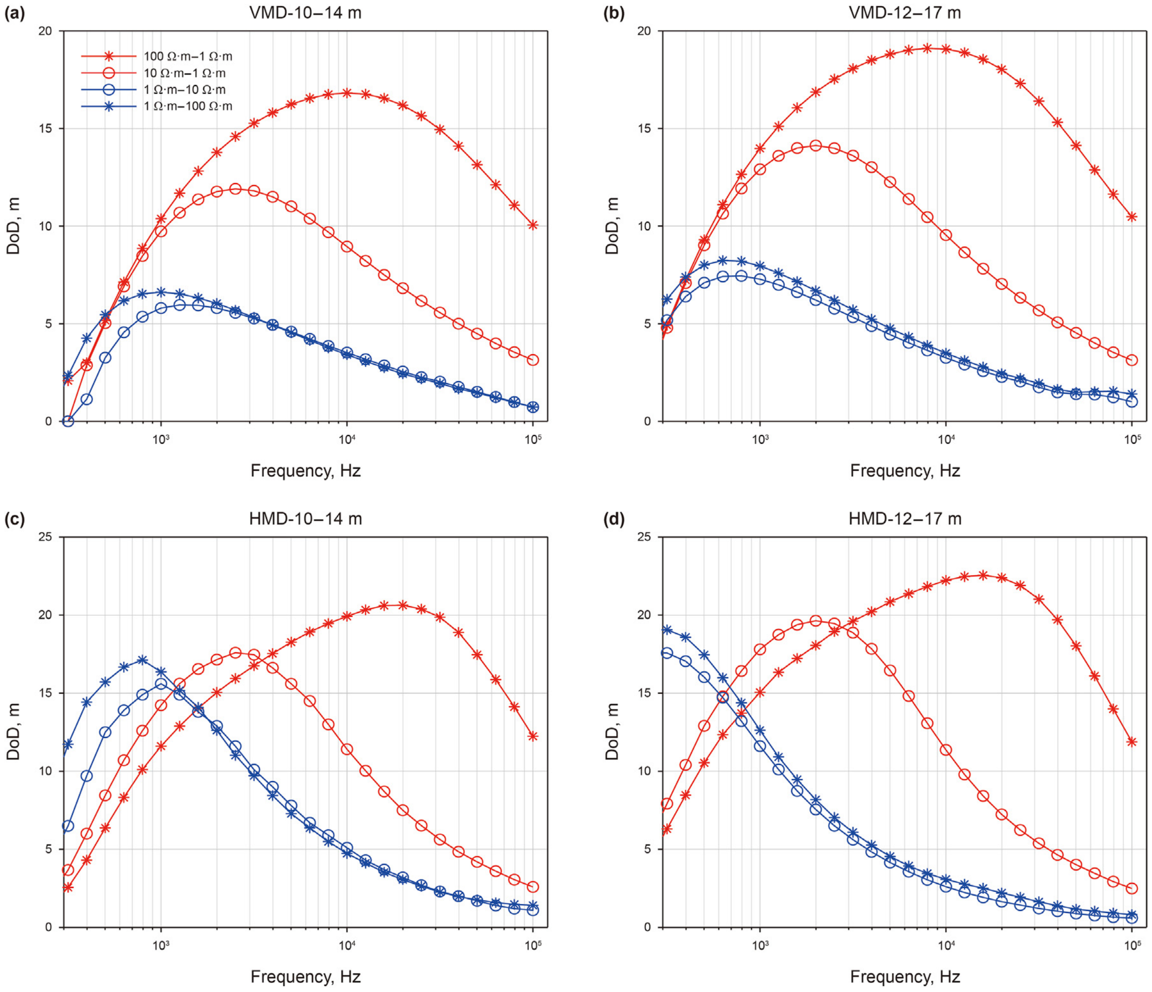

Fig. 8. DoD corresponds to the frequency in different models, (**a**)–(**b**) for VMD and (**c**)–(**d**) for HMD.

considering the strength of the received signals, the resolution provided at 20 kHz is preferable to that provide at 5 kHz. Consequently, the results of the computational analysis allow for the selection of different frequencies and TR combinations based on the specific geological conditions in a given area. This approach enables the use of various indicators to improve the detection depth and enhance the effectiveness of geological guidance.

3. Validation of instrument detection capability

The TR distance and frequency are determined, as described in the previous section. In this section, we have compared the consistency between the measured and simulated signal strengths and assessed the detection capability. Currently, there is limited information on the testing methods for evaluating the DoD of look-ahead electromagnetic resistivity instruments. A conventional method involves the use of a water tank for testing (Wang, 2023). However, because of the considerable length of the electromagnetic wave instruments, establishing a water tank testing environment spanning tens of meters is impractical. Another approach is to adapt the testing method used for directional electromagnetic resistivity instruments and perform tests on an air-sea dual-layer interface (Li et al., 2022). The conductivity of seawater makes it an ideal medium because of its extensive surface area, which meets the interface conditions. Its uniform properties simplify the numerical models and ensure consistency between the forward modeling and measurement environments. However, look-ahead instruments cannot directly use the same testing conditions as directional electromagnetic instruments. This is because the detection range of the look-ahead instrument is larger. The metal arms used during the measurement process and the seabed mud are within the detection range. These factors may have affected the received signals. In this section, we have outlined the conditions for mitigating the influence of the metal arms. We have calculated the test conditions to approximate a three-layer model (air-seawater-mud) as a two-layer model (air-seawater). This ensures consistency between the test and theoretical models used to evaluate the detection capability of the look-ahead instrument.

3.1. Consistency verification

Both the transmitter and receiver antenna use identical configurations, each consisting of 200-turn coils with a radius of 0.1 m and an input current of 1A. The transceiver antenna is wound onto two substrates of a metal drill collar positioned in a parallel configuration. In Fig. 11, the transmitting antenna remains fixes at the origin along the axial position, whereas the receiving antenna varies from 6 to 18 m. In Fig. 12, the blue curve represents the

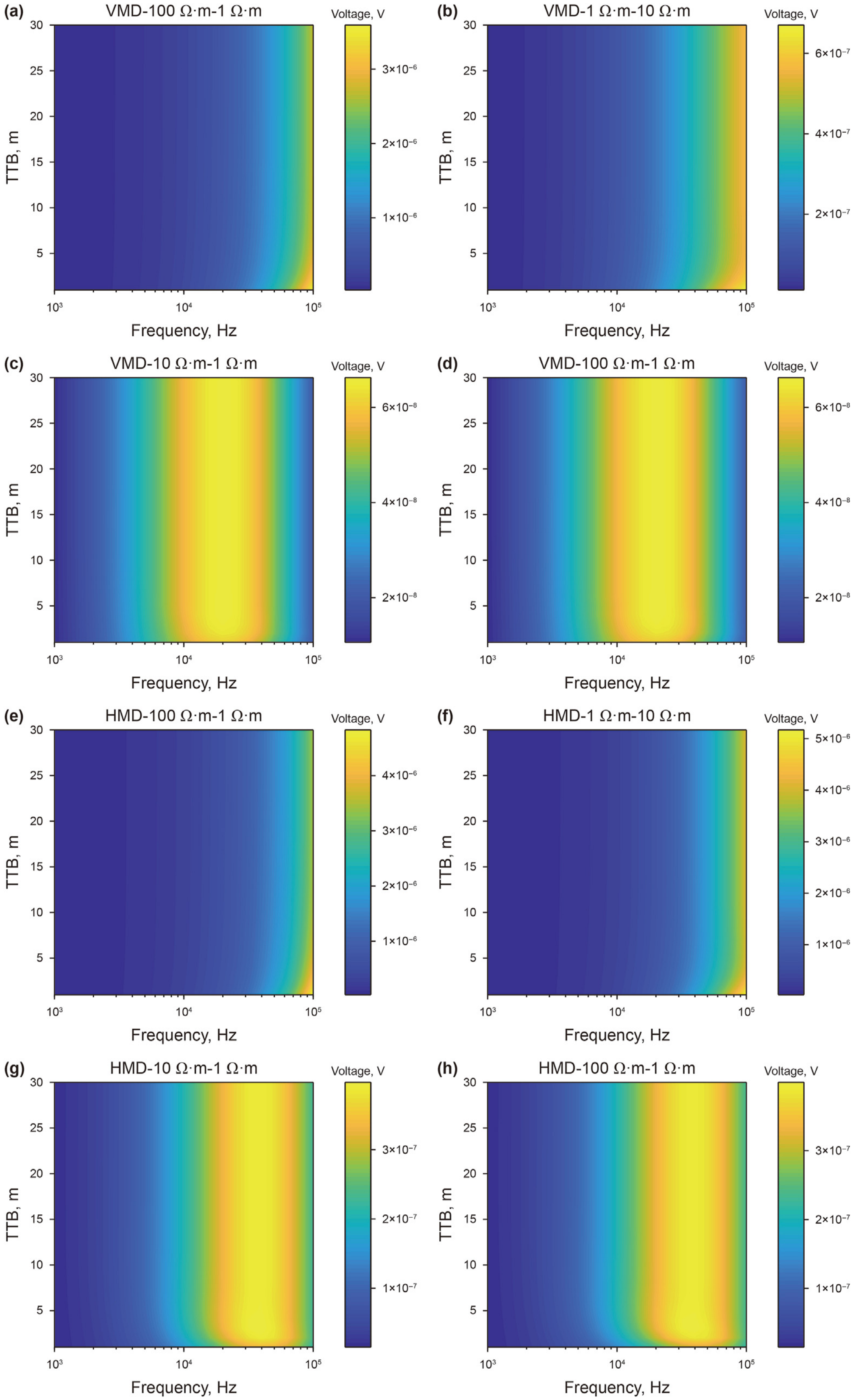

Fig. 9. Amplitude corresponds to the frequency in different models, (**a**)–(**b**) for VMD and (**c**)–(**d**) for HMD.

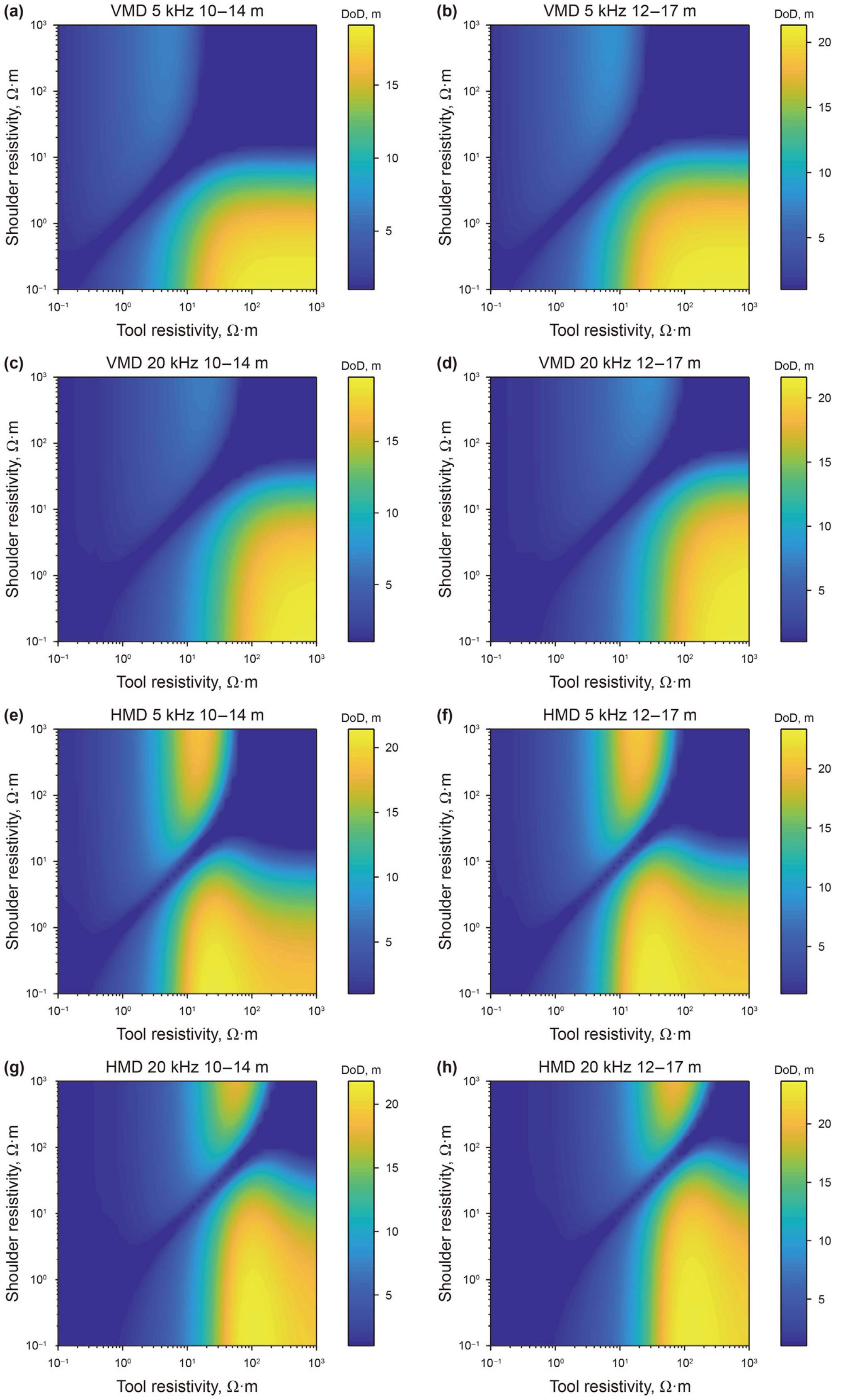

Fig. 10. DoD corresponds to the resistivity. (**a**)–(**d**) Variation of the 5 kHz DoD with λ, (**e**)–(**h**) Variation in the 20 kHz DoD with λ.

Fig. 11. Ground test: amplitude signals of the subs instrument at different TR distances.

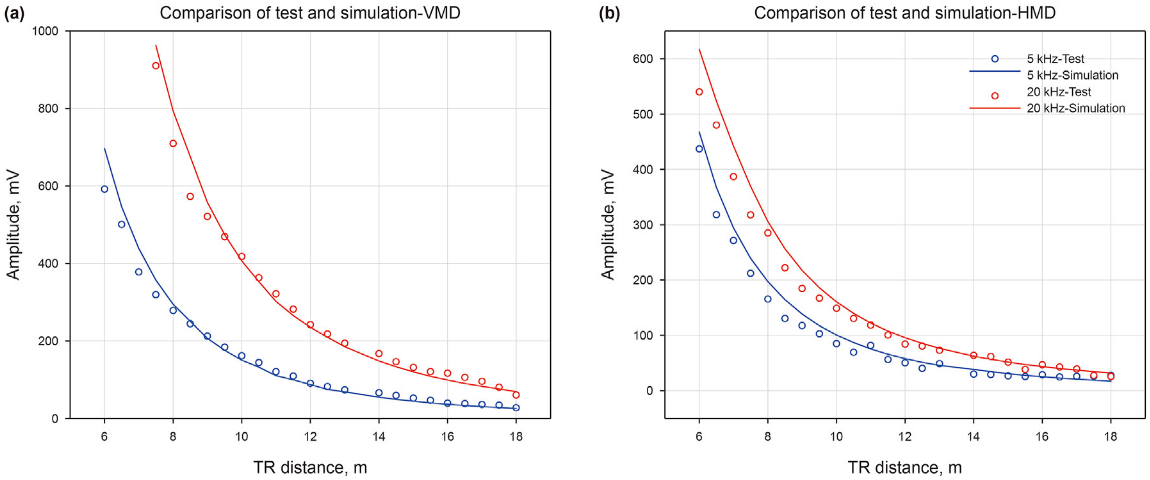

Fig. 12. Comparison of consistency between physical and simulation models. (**a**) VMD with 5 and 20 kHz, (**b**) HMD with 5 and 20 kHz.

calculated results at 5 kHz, the red curve represents those at 20 kHz, and the circles represent the test data. The results are generally in line with the simulated calculations. The received signal strength at 20 kHz is greater than that at 5 kHz but decays more rapidly. The amplitude of the received signal exhibits exponential decay with the TR distance, a characteristic of performance in high-resistivity formations, with VMD showing a higher signal strength than HMD. This confirms the reliability and practicality of the numerical simulations discussed in the previous section.

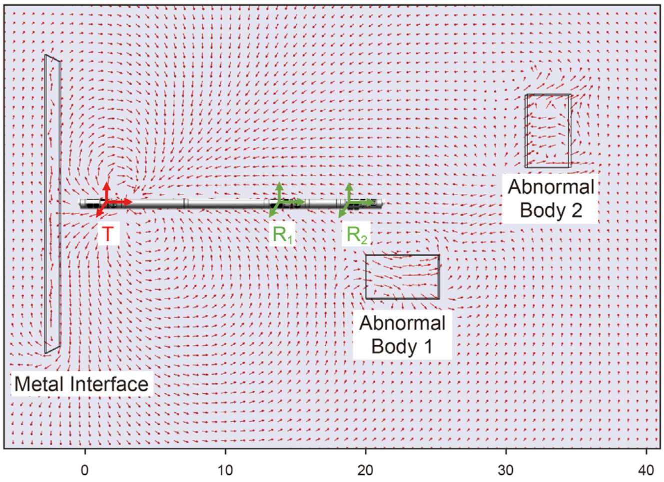

Fig. 13. The whole instrument testing model, where the anomalies are located at 20 and 34 m.

In Fig. 13, the TR is connected using a non-magnetic collar. The distances between T-R1 (#1) and T-R2 (#2) are 12 and 17 m, respectively. The apparatus is suspended 2.5 m above the ground with the metal reflection interface marked at 0 m. During the test, the entire device is moved in 1 m increments from 3 to 30 m. The test environment includes low-resistance anomalies located at 20 and 34 m. The spatial distribution of the electric field affected by these anomalies and boundaries is shown in Fig. 13. The reflective interface and anomalous bodies can be considered ideal conductors, situated 1.5 m from the axis. The normalized arrows represent the density and direction of the electric field at various points.

A comparison between the test and simulated data is shown in Fig. 14. The simulation results are not suitable with the anomalous bodies. Theoretically, if only the influence of the interface is considered, the electric field density should converge toward the interface and act as a conductive medium. Therefore, the results should align with the solid line in the figure. The actual received signal is smaller close to the interface, and gradually increases as the device moves away from it. The signal strength gradually approaches that of the uniform space. Fig. 14(a) shows that the outcomes for sub #1 are not influenced by anomalies, which is consistent with the simulation results for the initial 8 m. This demonstrates the consistency between the physical and simulation models.

The actual data curves are affected by the low-resistance bodies in the test environment. When TTB is 3 m, TR_2 is already within the influence of anomalous body 1. Consequently, the actual received signal for sub # 2 is stronger than the theoretical signal. As the tool moves further from the interface, the reception of sub # 2 increasingly aligns with the position of anomalous body 1. The

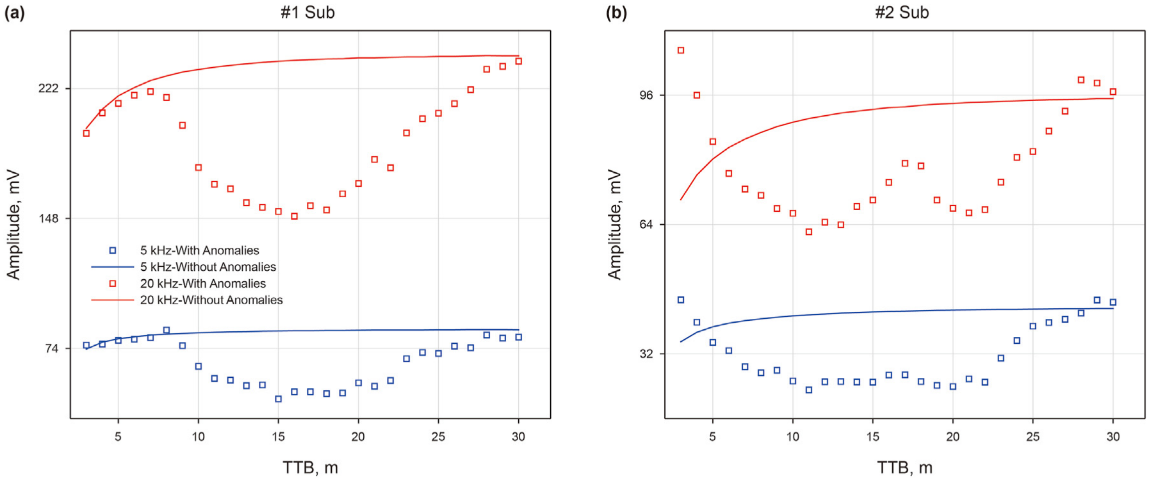

Fig. 14. Influence of low-resistivity anomalies on the received signal of the instrument. The solid line represents the signal response without anomalies, while the dashed line represents the measured signal with anomaly inclusion.

measured curve does not show an upward trend but gradually decreases until intersecting anomaly body 1, corresponding to the curve changes observed from 3 to 17 m in Fig. 14(b). The depression observed in the measured curve for sub #1 is also affected by anomalous body 1. However, owing to the shorter TR distance of 12 m, it remained outside the influence range of anomalous body 1 at the start. Consequently, the curve remained consistent with the simulation results, showing an initial upward trend. The effect of anomalous body 1 becomes apparent with a delay of approximately 5 m. Similarly, the effects of anomaly body 2 on the reception of the two short subs are discerned in the curves, which exhibit similar trends.

Fig. 14 shows the presence of anomalous bodies surrounding the instrument. The area affected by receiving antenna is extensive, making it challenging to determine the exact locations and sizes of the anomalies. To further illustrate this issue, Fig. 15 presents the amplitude ratios for two different frequencies. The effect of the anomalies is more apparent in the amplitude ratio curve. The amplitude ratio curve has a downward trend in the absence of anomalies in the test environment. The sections of the curve that rise correspond to areas in which the instrument is influenced by anomalous bodies. Although the amplitude ratio curve cannot pinpoint the exact location of the anomalies, it can indicate their length along the path. In summary, the processed data exhibits amplitude discrimination capabilities. The variation in the signal intensity with the interface distance aligns with the structural characteristics of the instrument. The instrument can distinguish between interfaces and anomalies with significant contrast in the test environment. These results are used to analyze the impact of the air-sea test environment on the instrument.

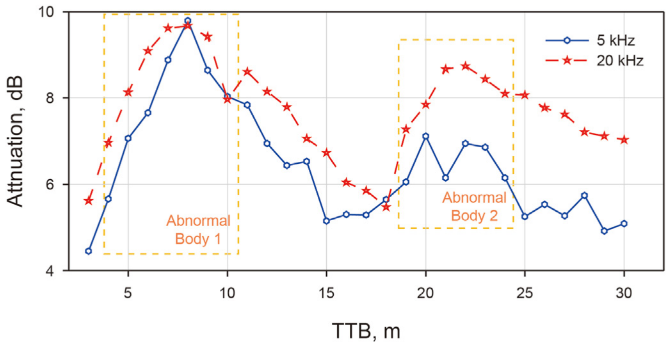

Fig. 15. Impact of low-resistivity anomalies on the amplitude ratio, with the box corresponding to the position of the two anomalies.

3.2. *Ideal conditions for air-sea testing*

The air-sea test model is illustrated in Fig. 16. The tail end of the metal arm is situated on the shore, with the highest suspension point positioned 30 m above the receiving antenna. The horizontal distance between the suspension point and shoreline is represented by *D*. As discussed in the previous section, the metal arm can be considered a low-resistance anomaly in the testing environment. If the metal arm can not affect the received signal when vertically suspended at its highest point, it should not affect the signal during descent.

In this model, the received signal strength is calculated at different frequencies, excluding the metal arms. Fig. 17 illustrates the amplitude with *D*. It is assumed that the variation is not exceed 1%, indicating that the test conditions are suitable. At a frequency of 20 kHz, a *D* greater than 32 m meets the test requirements. At 5 kHz, the frequency must exceed 35 m to ensure that the received signal is unaffected by the metal arm. According to the relationship between the lift height and *D*, this condition satisfies the test environment requirements while ensuring safety.

Fig. 18 illustrates the schematic diagrams of the air-sea two-layer model and the air-sea-mud three-layer model, with the second layer having a resistivity of 0.2 $\Omega\cdot$m and the third layer having a resistivity of 100 $\Omega\cdot$m. Given that the test environment is the three-layer model, the detection capability is calculated using the two-layer model. The consistency between the results from the two models helps to determine the approximate conditions for both the test and theoretical models. Under these conditions, the calibration test results are more accurate.

The received signal strengths at TR distances of 10 m, with TTB of 2, 5, and 10 m, are compared with the calculations from the two-layer model. In Fig. 19, the dashed lines represent the signal amplitudes from the two-layer model. The solid circles denote the calculated results from the three-layer model with the same TTB. This indicates that the influence of intermediate depth on the received signal is relatively small when the tool is positioned farther from the sea surface. For a frequency of 5 kHz, a TTB of 2 m requires a sea depth of at least 6 m to ensure the model accuracy.

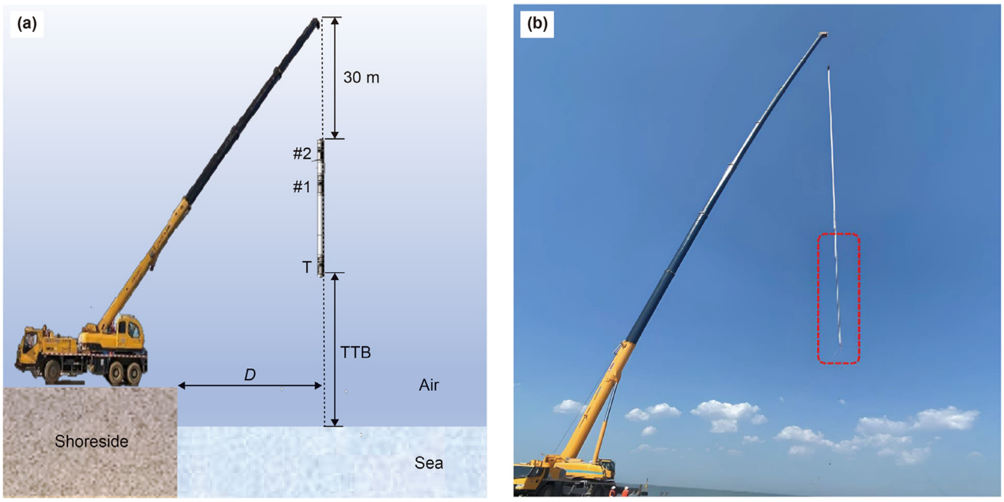

Fig. 16. The model of air-sea hang testing. (**a**) Illustration of the sea-level testing suspension structure and environment. (**b**) Test setup with the instrument suspended above the sea surface during the air-sea hanging test. The red circles indicate the hanging well logging instrument in the air on the sea surface.

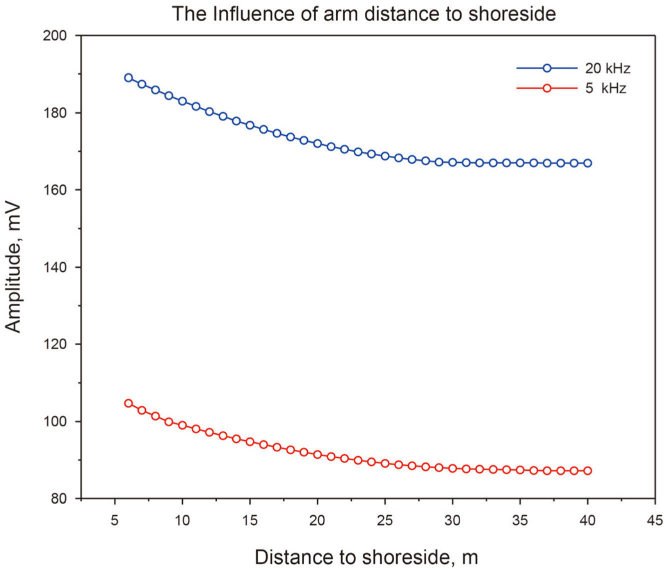

Fig. 17. Effect of metal suspension arms on received signals.

When the TTB is 10 m, a sea depth of 2 m is sufficient to achieve the desired level of accuracy. At a frequency of 20 kHz, the sea depth requirements are even lower because high-frequency signals attenuate more rapidly in water.

The analysis method for the other TR distances is the same as described. Table 1 presents the approximate conditions that must be satisfied for each TR distance and frequency. It shows that the approximate conditions for these TR distances are consistent. Under relatively strict approximation criteria, the seawater depth of 7 m provided satisfactory approximation results. Therefore, when selecting experimental locations, the influence of local tides on seawater depth must also be considered.

3.3. Detection capability of the instrument

We evaluate the look-ahead detection capability of the instrument using two TR combinations, that is, 10–14 m and 12–17 m, at frequencies of 5 and 20 kHz. The horizontal antenna has the same number of turns as the axial antenna. However, its coil area is smaller because of the constraints imposed by the antenna slot structure. TTB is sequentially reduced from 30 to 1 m. The test results are compared with the simulation results (Fig. 20). The left and right axes represent the signal intensity, and amplitude ratio, and the horizontal axis represents TTB. TR_1 denotes the short-distance sub and TR_2 denotes the long-distance sub.

The trend shows that the VMD signal increases, whereas the HMD signal decreases as TTB increased. The measured signal intensity align closely with the simulation results, with VMD data demonstrating greater stability than HMD data. For the 20 kHz and short-distance configurations, the quality of the measured data is superior to that of the 5 kHz and long-distance configurations. A higher frequency and shorter TR distance result in increased received signal intensity, thereby mitigating the impact of noise within the same testing environment. We use the normalized amplitude ratio signal to evaluate detection capability. However, this ratio highlights the signal decay characteristics and amplifies noise effects. Although the experimental amplitude ratio trend aligned with the theoretical curve, there is a discrepancy in the amplitude magnitudes. This is particularly evident in the HMD-5kHz amplitude ratio, which displays a negligible change and deviates significantly from the theoretical value. The ambient noise level is approximately 20 mV, and the effective amplitude of the HMD-5kHz signal is comparable to this noise level. The amplitude ratio provides fewer effective signal instances and more reflections of background noise fluctuations.

The model illustrates in Fig. 18(a) is used for the air-sea test. The previously provided numerical simulation results are based on a standard stratigraphic model with $\lambda = 100$, as is common in the industry. To determine whether sea test results align with expectations, they must be converted into a standard theoretical model. Fig. 21 illustrates the conversion between the test and standard models. The HMD-5kHz measurements across the various models are consistent and there is no need to further conversion. Therefore, the test results directly represent the standard DoD. However, the DoD at 20 kHz in the test model is slightly higher than that in the standard model. For VMD, the difference between the two models is approximately 3 m. Therefore, the test results must be adjusted by subtracting the corresponding differences to match industry-defined look-ahead detection distances.

The relative errors between the adjusted sea test results and the

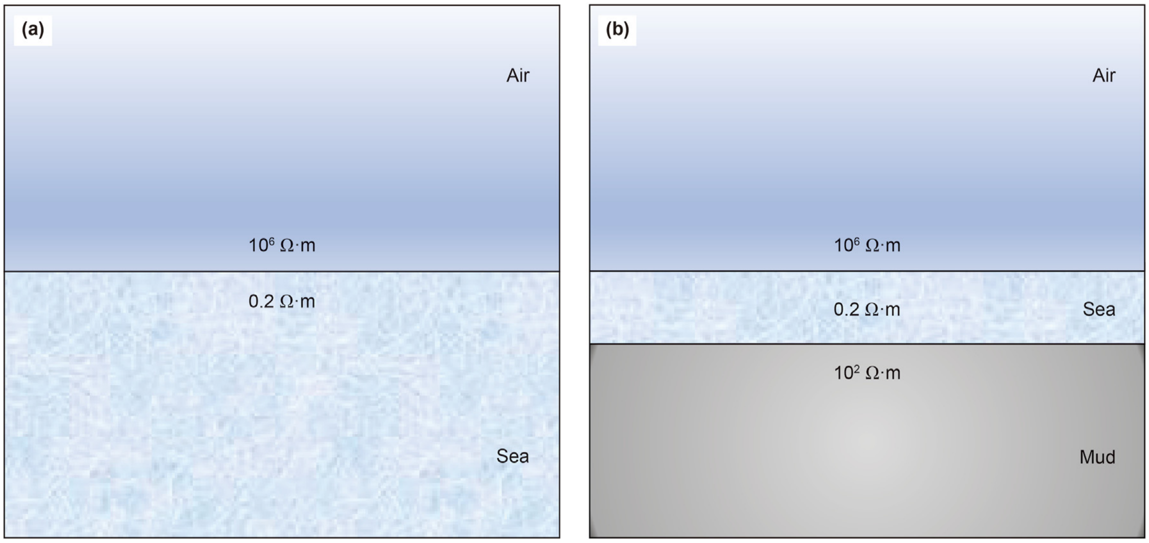

Fig. 18. Theoretical and practical test models. (**a**) Air-sea water two-layer model. (**b**) Air-sea water-mud three-layer model.

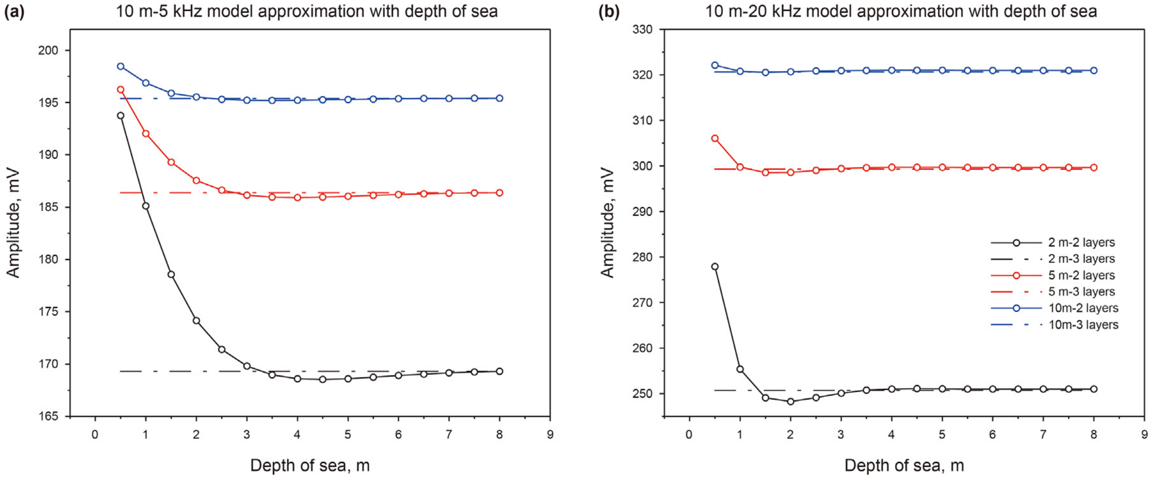

Fig. 19. Comparison of different seawater depths with two-layer model. (**a**) Calculation results for 10 m-5 kHz, (**b**) Calculation results for 10 m-20 kHz.

Table 1
Approximate conditions for different TR distances and frequencies.

TR, m	10		12		14		17	
Freq, kHz	5	20	5	20	5	20	5	20
TTB = 2 m	7.0 m	3.5 m	7.0 m	3.5 m	7.0 m	3.5 m	7.0 m	3.5 m
TTB = 5 m	6.0 m	3.0 m	6.0 m	3.0 m	6.5 m	3.5 m	6.5 m	3.5 m
TTB = 10 m	2.0 m	2.0 m	2.0 m	1.0 m	2.0 m	3.0 m	2.0 m	2.5 m

standard model are presented in Tables 2 and 3, with “S” indicating the short-distance combination (10–14 m) and “L” indicating the long-distance combination (12–17 m). The last row shows the error between the converted DoD and simulation results. In this test model, the signal strength of VMD is marginally higher than that of HMD. Comparing the detection capabilities of both signal components at the higher quality 20 kHz frequency, the DoD for VMD with the short-source distance is approximately 15.22 m. The long-source distance is approximately 17.80 m. For HMD, the maximum detection depth is marginally higher than for VMD, with a short-source DoD of approximately 19.76 m and a long-source DoD of around 21.61 m. The relative errors between the converted DoD and theoretical values are within a suitable range. This confirms that the results are consistent with the simulation calculations.

The test results highlight the significance of integrating numerical simulations with instrument design to achieve an enhanced detection depth. Using the amplitude ratio of HMD-5kHz theoretically provides a greater detection depth compared to VMD-20kHz. However, the device could not capture the strength of the effective signals at low frequencies further from the interface. Consequently, the results are not as favorable as those at 20 kHz. The receiving area of the horizontal antenna is smaller than that of the vertical antenna. Consequently, the received signal strength of HMD is lower than that VMD. If the received signal strength significantly exceeds the noise level, the simulation results suggest that low frequency, long TR distances, and the horizontal component of the signal can be used as indicators to achieve a greater detection depth. To enhance the signal amplitude, the slot for the horizontal antenna must be optimized to balance mechanical strength with performance. Hence, optimizing the structure of the loop antenna can improve radiation efficiency. Conversely, the

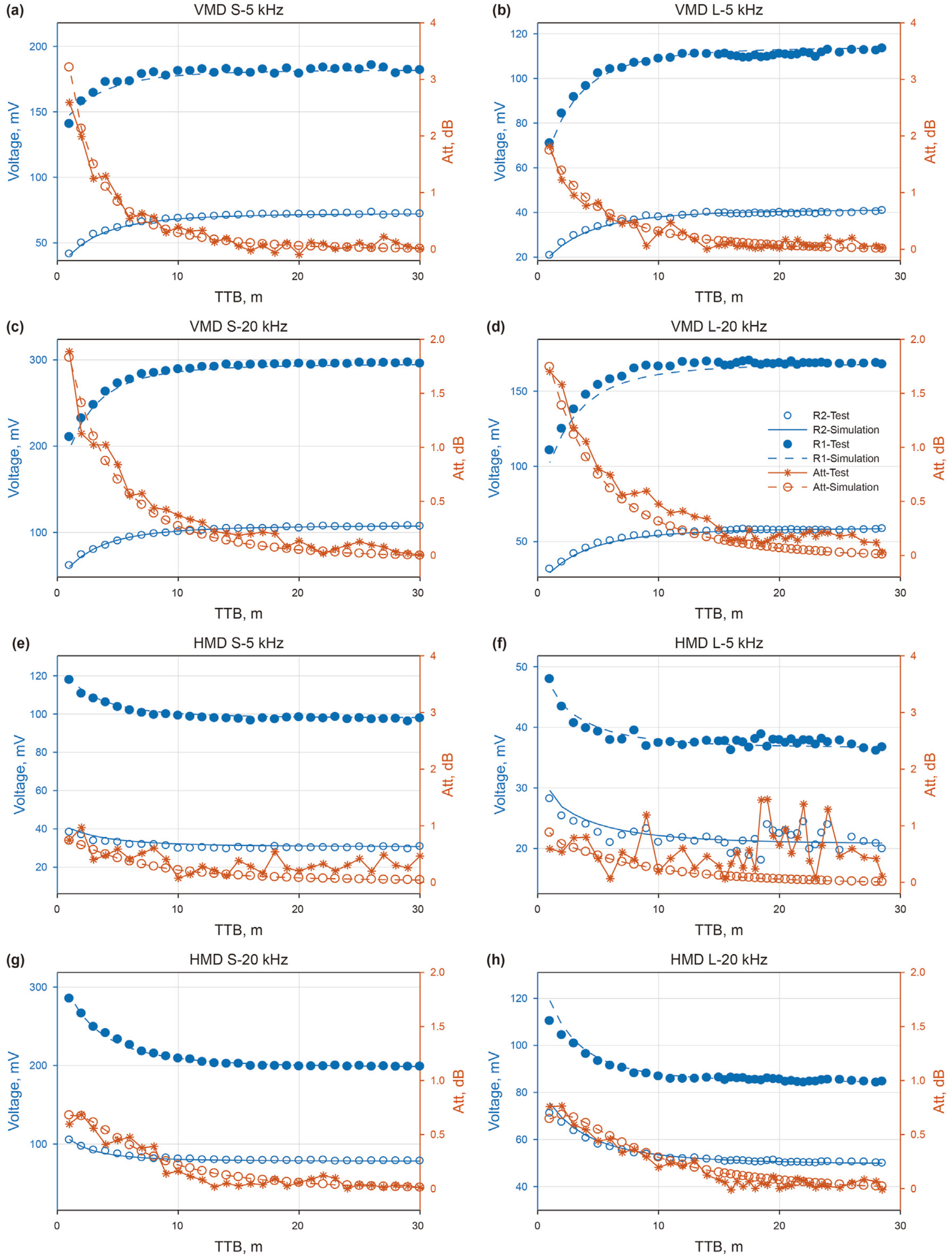

Fig. 20. Signal amplitude and magnitude ratio of the test results. (**a**)–(**d**) Comparison of test and simulation results for VMD. (**e**)–(**h**) Comparison of test and simulation results for HMD. Blue indicates the received signal amplitude, and orange represents the amplitude ratio.

15–30 m range is crucial in the amplitude ratio curve because it primarily affects the resolution of the device in the weak signal range. Therefore, optimizing the denoising technology can mitigate its impact on the effective signals.

4. Conclusion

In this study, magnetic dipoles are used as both transmitter and receiver antenna, and the electromagnetic response is computed in a TI medium. The coaxial component is chosen as the indicator of the detection capability by comparing the sensitivities of various

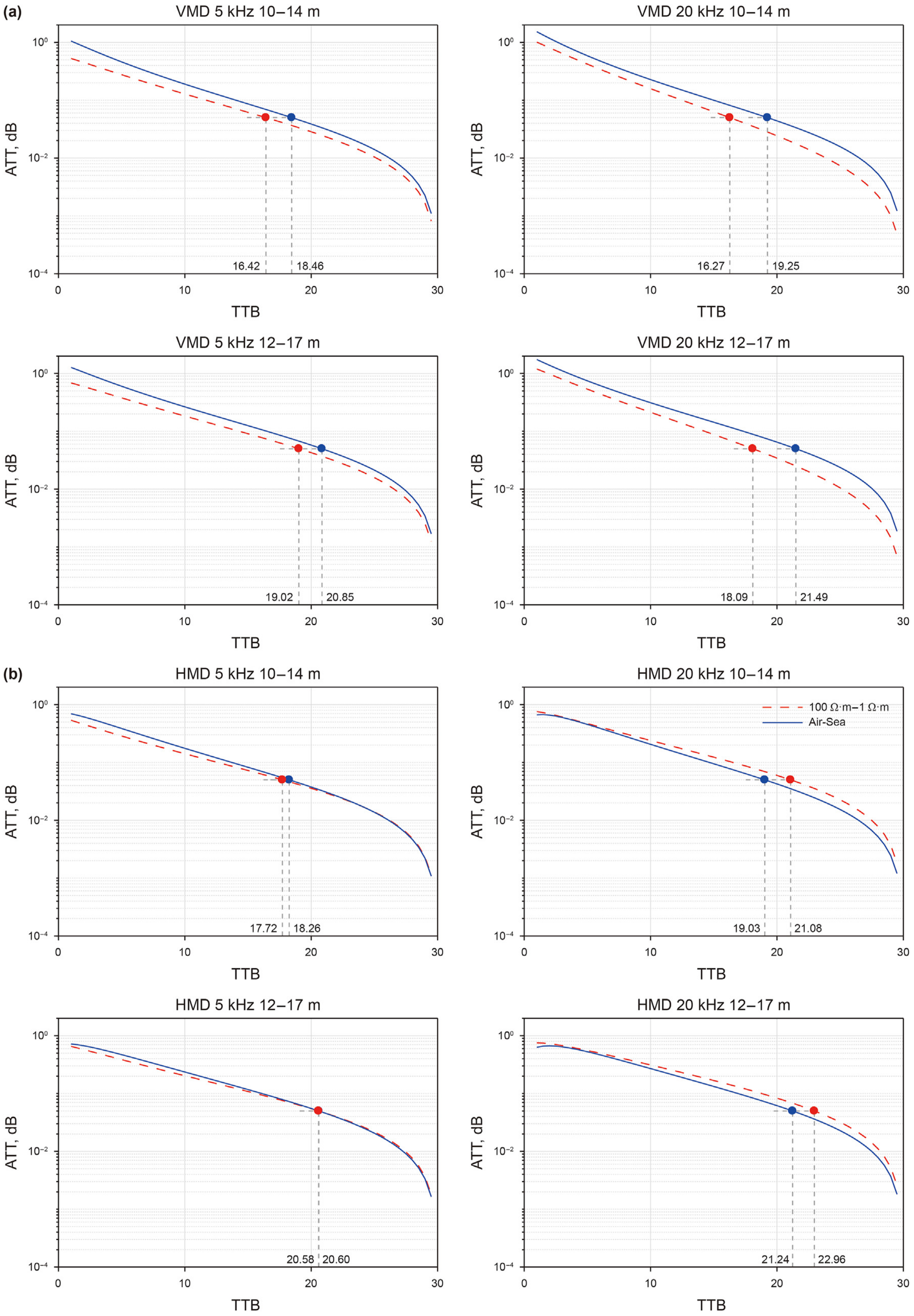

Fig. 21. Conversion plates for different combinations of the instrument. (**a**) VMD Air-sea testing and standard modeling conversion plate. (**b**) HMD Air-sea testing and standard modeling conversion plate.

Table 2
Comparison of converted VMD test results with the standard model.

	S-5 kHz		S-20 kHz		L-5 kHz		L-20 kHz	
Model	Air-Sea	Simulation	Air-Sea	Simulation	Air-Sea	Simulation	Air-Sea	Simulation
DoD, m	15.52	16.42	15.22	16.27	17.96	19.02	17.80	18.09
Error	5.48%		6.45%		5.57%		1.60%	

Table 3
Comparison of converted HMD test results with the standard model.

	S-5 kHz		S-20 kHz		L-5 kHz		L-20 kHz	
Model	Air-Sea	Simulation	Air-Sea	Simulation	Air-Sea	Simulation	Air-Sea	Simulation
DoD, m	16.67	17.72	19.76	21.08	19.46	20.58	21.61	22.96
Error	5.92%		6.26%		5.44%		5.87%	

magnetic dipole components to the axial information. We analyze the effects of variations in the formation models, including the TR distance, frequency, and resistivity, on the intensity of the received signals and DoD.

Considering the minimum resolution of the instrument and the threshold for detecting effective signals, two sets of TR distance combinations of 10–14 m and 12–17 m have been proposed. Therefore, the effectiveness and practicality of the numerical calculations are verified. A sea test is conducted to assess the detection capability of the tool at 5 and 20 kHz. A testing model is also proposed that is suitable for calibrating the DoD of look-ahead instruments. The results indicate that the tool can identify the boundary at a distance of 21.6 m in a high-resistance environment.

CRediT authorship contribution statement

Ran-Ming Liu: Writing – original draft, Validation, Methodology. **Wen-Xiu Zhang:** Writing – review & editing. **Wen-Xuan Chen:** Writing – review & editing. **Peng-Fei Liang:** Writing – review & editing, Methodology. **Xing-Han Li:** Writing – review & editing, Data curation. **Zhi-Xiong Tong:** Writing – review & editing.

Declaration of competing interest

The authors declare that they have no known competing financial interests or personal relationships that could have appeared to influence the work reported in this paper.

Acknowledgements

This research has been co-funded by the National Key Research and Development Program of China under Grant (2019YFA0708301), the CAS Project for Young Scientists in Basic Research (Grant No. YSBR-082) and Research Instrument and Equipment Development Project of Chinese Academy of Sciences (GJJSTD20210008).

References

Bittar, M.S., 2009. A new azimuthal deep-reading resistivity tool for geosteering and advanced formation evaluation. SPE Reservoir Eval. Eng. 12 (2), 270–279. https://doi.org/10.2118/109971-PA.

Bittar, M.S., 2000. Electromagnetic Wave Resistivity Tool Having a Tilted Antenna for Determining the Horizontal and Vertical Resistivities and Relative Dip Angle in Anisotropic Earth Formations. US007557579B2.

Constable, M.V., Antonsen, F., Olsen, P.A., et al., 2012. Improving well placement and reservoir characterization with deep directional resistivity measurements. SPE Annual Technical Conference and Exhibition. https://doi.org/10.2118/159621-MS. San Antonio, Texas, USA. p. SPE-159621.

Constable, M.V., Antonsen, F., Stalheim, S.O., et al., 2016. Looking ahead of the bit while drilling: from vision to reality. SPWLA 57th Annual Logging Symposium. Reykjavik, Iceland. SPWLA-2016.

Fan, J., Zhang, W., Chen, W., et al., 2021. Electric and magnetic dipole antennas of a directional resistivity logging-while-drilling tool for "look-around" boundary detection. Geophysics 86, D215–D239. https://doi.org/10.1190/geo2020-0679.1.

Guo, Q.B., Hao, X., Wu, C., et al., 2020. Deep EM method for proactively prediction of resistivity ahead of bit to determine salt bottom position. International Petroleum Technology Conference, Dhahran, Kingdom of Saudi Arabia. IPTC-19616. https://doi.org/10.2523/IPTC-19616-Abstract.

Hong, D.C., Yang, S.W., Zhang, Y., et al., 2018. Pseudoanalytical formulations for modeling the effect of an insulating layer in electromagnetic well logging. IEEE Trans. Geosci. Rem. Sens. 56, 7022–7029. https://doi.org/10.1109/TGRS.2018.2847027.

Huang, M., Shen, L.C., 1989. Computation of induction logs in multiple-layer dipping formation. IEEE Trans. Geosci. Rem. Sens. 27, 259–267. https://doi.org/10.1109/36.17667.

Larsen, D., Antonov, Y., Luxey, P., et al., 2016. Navigating the horizontal section in a heterogeneous formation while using extra deep azimuthal resistivity for optimizing the wellbore placement within a narrow TVD window. SPWLA 57th Annual Logging Symposium. SPWLA-2016.

Li, Q.M., Omeragic, D., Chou, L., et al., 2005. New directional electromagnetic tool for proactive geosteering and accurate formation evaluation while drilling. SPWLA 46th Annual Logging Symposium. New Orleans, Louisiana, United States. SPWLA-2005.

Li, W., Chen, J.B., Jin, B.Q., et al., 2019. Ultra-deep high definition reservoir mapping while drilling measurement to optimize landing operation: a case study from offshore China. SPWLA 25th Formation Evaluation Symposium. Japan, Chiba. p. SPWLA-JFES-2019.

Li, X.H., Zhang, W.X., Chen, P., et al., 2022. Calibration method of azimuth electromagnetic boundary detection logging while drilling based on air–seawater double-layer dielectric as reflection interface. J. Geophys. Eng. 19, 681–693. https://doi.org/10.1093/jge/gxac043.

Liang, P.F., Di, Q.Y., Chen, W.X., et al., 2023. An EM LWD tool for deep reading looking-ahead. IEEE Access 11, 142601–142610. https://doi.org/10.1109/ACCESS.2023.3339777.

Lin, X., Yuan, R.G., Qin, L., et al., 2021. Present situation and progress of geosteering drilling pre-prospecting technology. Special Oil Gas Reservoirs 28, 1–10. https://doi.org/10.3969/j.issn.1006-6535.2021.02.001 (in Chinese).

Liu, R.M., Zhang, W.X., Chen, W.X., et al., 2024. Analysis and experimental research on the factors affecting downhole inductive electromagnetic wave wireless short-hop transmission. IEEE Trans. Geosci. Rem. Sens. 62, 1–11. https://doi.org/10.1109/TGRS.2024.3398030.

Meador, R.A., 2009. Logging-while-drilling a story of dreams, accomplishments, and bright futures. SPWLA 50th Annual Logging Symposium. The Woodlands, Texas SPWLA-2009.

Meyer, W.H., Thompson, L.W., Wisler, M.M., et al., 1994. A new slimhole multiple propagation resistivity tool. SPWLA 35th Annual Logging Symposium. Tulsa, Oklahoma.

Omeragic, D., Research, S.D., Li, Q., et al., 2005. Deep directional electromagnetic measurements for optimal well placement. SPE Annual Technical Conference and Exhibition. Dallas, Texas, p. SPE 97045. https://doi.org/10.2118/97045-MS.

Pardo, D., Torres Verdín, C., 2015. Fast 1D inversion of logging-while-drilling resistivity measurements for improved estimation of formation resistivity in high-angle and horizontal wells. Geophysics 80, E111–E124. https://doi.org/10.1190/geo2014-0211.1.

Seydoux, J., Legendre, E., Mirto, E., et al., 2014. Full 3D deep directional resistivity measurements optimize well placement and provide reservoir-scale imaging while drilling. SPWLA 55th Annual Logging Symposium. Abu Dhabi, United Arab Emirates. p. SPWLA-2014.

Su, Y.N., 2005. Geosteering drilling technology and its development in China. Petrol. Explor. Dev. 32 (1), 92–95. https://doi.org/10.3321/j.issn:1000-0747.2005.01.025.

Teruhiko, H., Song, H., 2001. Directional resistivity measurements for azimuthal proximity detection of bed boundaries. USOO6181138B1.

Upchurch, E.R., Saleem, S., Russell, K., et al., 2015. Geo-stopping using deep directional resistivity LWD: a new method for well bore placement using below-the-bit resistivity mapping. SPE/IADC Drilling Conference and Exhibition, London, England, UK. D011S006R006. https://doi.org/10.2118/173169-MS.

Wang, H.N., 2011. Adaptive regularization iterative inversion of array multicomponent induction well logging datum in a horizontally stratified inhomogeneous TI formation. IEEE Trans. Geosci. Rem. Sens. 49, 4483–4492. https://doi.org/10.1109/TGRS.2011.2142187.

Wang, L., Deng, S.G., Xie, G.B., et al., 2022. A new deep-reading look-ahead method in electromagnetic logging-while-drilling using the scattered electric field from magnetic dipole antennas. Petrol. Sci. 19, 180–188. https://doi.org/10.1016/j.petsci.2021.09.035.

Wang, L., Deng, S.G., Zhang, P., et al., 2019. Detection performance and inversion processing of logging-while-drilling extra-deep azimuthal resistivity measurements. Petrol. Sci. 16, 1015–1027. https://doi.org/10.1007/s12182-019-00374-4.

Wang, L., Li, S.J., Fan, Y.R., 2020. An all-new ultradeep detection method based on hybrid dipole antennas in electromagnetic logging while drilling. IEEE Trans. Geosci. Rem. Sens. 58, 2124–2134. https://doi.org/10.1109/TGRS.2019.2953304.

Wang, T., 2023. Field testing of a propagation at-bit resistivity tool. SPWLA 64th Annual Logging Symposium, Lake Conroe, TX, USA. https://doi.org/10.30632/SPWLA-2023-0122.

Yu, L., Wang, H.N., Wang, H.S., et al., 2022. 3-D finite volume modeling for LWD azimuthal propagation resistivity tool with multiple annular antenna recesses using coupled potentials on cylindrical grids. IEEE Trans. Antennas Propagat. 70, 514–525. https://doi.org/10.1109/TAP.2021.3098522.

Zhang, C., Liu, G.Q., Xia, Z.W., et al., 2018. Frequency and space selection method for long space directional electromagnetic logging while drilling tools. Transactions of China Electrotechnical Society 33, 4756–4762. https://doi.org/10.19595/j.cnki.1000-6753.tces.180283 (in Chinese).

Zhang, Z.Y., Yu, L.M., Kriegshäuser, B., et al., 2004. Determination of relative angles and anisotropic resistivity using multicomponent induction logging data. Geophysics 69, 898–908. https://doi.org/10.1190/1.1778233.

Zhong, L.L., Li, J., Bhardwaj, A., et al., 2008. Computation of triaxial induction logging tools in layered anisotropic dipping formations. IEEE Trans. Geosci. Rem. Sens. 46, 1148–1163. https://doi.org/10.1109/TGRS.2008.915749.